Modelling and Simulation in Materials Science and Engineering

Effect of pre-existing immobile dislocations on the evolution of geometrically necessary dislocations during fatigue

To cite this article: Ainara Irastorza-Landa *et al* 2017 *Modelling Simul. Mater. Sci. Eng.* **25** 055010

OPEN ACCESS
IOP Publishing
Modelling and Simulation in Materials Science and Engineering
Modelling Simul. Mater. Sci. Eng. **25** (2017) 055010 (20pp) https://doi.org/10.1088/1361-651X/aa6e24

Effect of pre-existing immobile dislocations on the evolution of geometrically necessary dislocations during fatigue

Ainara Irastorza-Landa[1,2], Nicolò Grilli[1,3] and Helena Van Swygenhoven[1,2]

[1] NXMM Laboratory, IMX, École Polytechnique Fédéral Lausanne (EPFL), CH-1015 Lausanne, Switzerland
[2] Photons for Engineering and Manufacturing (PEM), SYN, Paul Scherrer Institut, CH-5232 Villigen PSI, Switzerland
[3] Laboratory for Nuclear Materials (LNM), NES, Paul Scherrer Institut, CH-5232 Villigen PSI, Switzerland

E-mail: helena.vanswygenhoven@psi.ch

Received 12 August 2016, revised 4 April 2017
Accepted for publication 20 April 2017
Published 23 May 2017

Abstract

The role of pre-existing mobile and immobile dislocation densities on the evolution of geometrical necessary dislocation densities (GNDs) during cyclic fatigue in shear is studied using a continuum dislocation-based model incorporated in a crystal plasticity finite element scheme. Clusters with different immobile dislocation densities are implemented in a homogeneous medium containing a certain mobile dislocation density. It is found that whether GND walls are formed around the initial immobile cluster (or not) strongly depends on the absolute values of initial mobile dislocation density and on the ratio between mobile and immobile densities. The results are discussed in terms of the apparent GND densities experimentally obtained using Laue micro-diffraction.

Keywords: crystal plasticity finite element, fatigue, initial dislocation densities, crystal rotation evolution

(Some figures may appear in colour only in the online journal)

1. Introduction

Cyclic fatigue of FCC metals is a phenomenon that leads to microstructural changes and eventually to material damage as a consequence of the accumulated plastic deformation caused by the to-and-fro motion of dislocations. These line defects interact and form dislocation patterns, whose characteristics are strongly dependent on the loading conditions [1]. During single slip cyclic deformation at low strain amplitude, the so-called 'vein-channel' structure forms [2]: veins are regions with high dislocation density constituted mainly of edge dislocations in the form of dipoles, while channels are almost empty of edge dislocations. During early stages of fatigue, the presence of pre-existing dislocation agglomerations represents a barrier for the motion of dislocations and opposite signed gliding dislocations can get blocked around these ensembles. This gives rise to crystal lattice curvatures which can be described by geometrically necessary dislocations (GND) [3]. It has been reported that in fatigued structures the GND density deposited at the perimeter of dipolar bundles is about 1% of the total dislocation density [4] and that they create a small misorientation around the line direction of the primary edge dislocation [5]. There is however a lack of quantitative data on the misorientation caused by a forming vein.

Computationally, the influence of pre-existing dislocation densities in fatigued samples has been addressed in relation to the sample size and/or the grain size. 3D-DDD simulations showed that there is a critical sample size of 2 μm below which no cell structures can be obtained in multiple slip oriented cycled single crystals independently of the initial dislocation density. For larger samples, a minimum dislocation density is required in order to form patterning. The patterning is observed to depend on the crystal size [6]. On the other hand, simulations performed with a reaction-diffusion 1D continuum model [7] suggested that no clear dislocation wall pattern is formed during cycling when the grain size is below 1 μm and the initial immobile dislocation density is 1 μm^{-2}. Under these conditions there are no immobile dislocations inside the grain. However, when keeping the same value of the immobile dislocation density but increasing the grain size, i.e. including immobile dislocations inside the grain, walls are formed first close to the grain boundary and then also inside the grain. These studies indicate that the presence of initial immobile dislocations plays a role in the early stages of fatigue; however they do not provide information on the spatial distribution of the lattice rotations.

Coupling 3D dislocation dynamics with a 3D finite element methods (FEM) allows to simulate the crystal lattice rotation induced by plastic deformation, using the polar decomposition of the elastic deformation gradient [8], as it has been shown for the 3D cell structures formed after monotonic uniaxial tensile loading [9–13]. The description of GND requires a constitutive model that takes into account the sign (positive or negative) of dislocation densities [14]. Recently dislocation-based rate equations have been implemented in a crystal plasticity FEM (CPFEM) scheme to reproduce dislocation structures during cyclic fatigue starting from a perfect single crystal [15]. A systematic investigation of the effect of initial immobile dislocation clusters on the evolution of lattice rotation during early fatigue with CPFEM models has not been performed though. In addition quantitative experimental data would be required to validate such simulations.

The evolution of the crystal rotation during early stages on cyclically deformed copper single crystal oriented for single slip was analyzed with Laue micro-diffraction in transmission mode [16]. A sample with gauge thickness of 30 μm was subjected to 120 shear cycles while applying a multiple step test methodology: the displacement amplitude was kept constant during a certain number of cycles and subsequently increased to a higher level before applying more cycles. Using a similar approach as in EBSD [17, 18], the local orientation

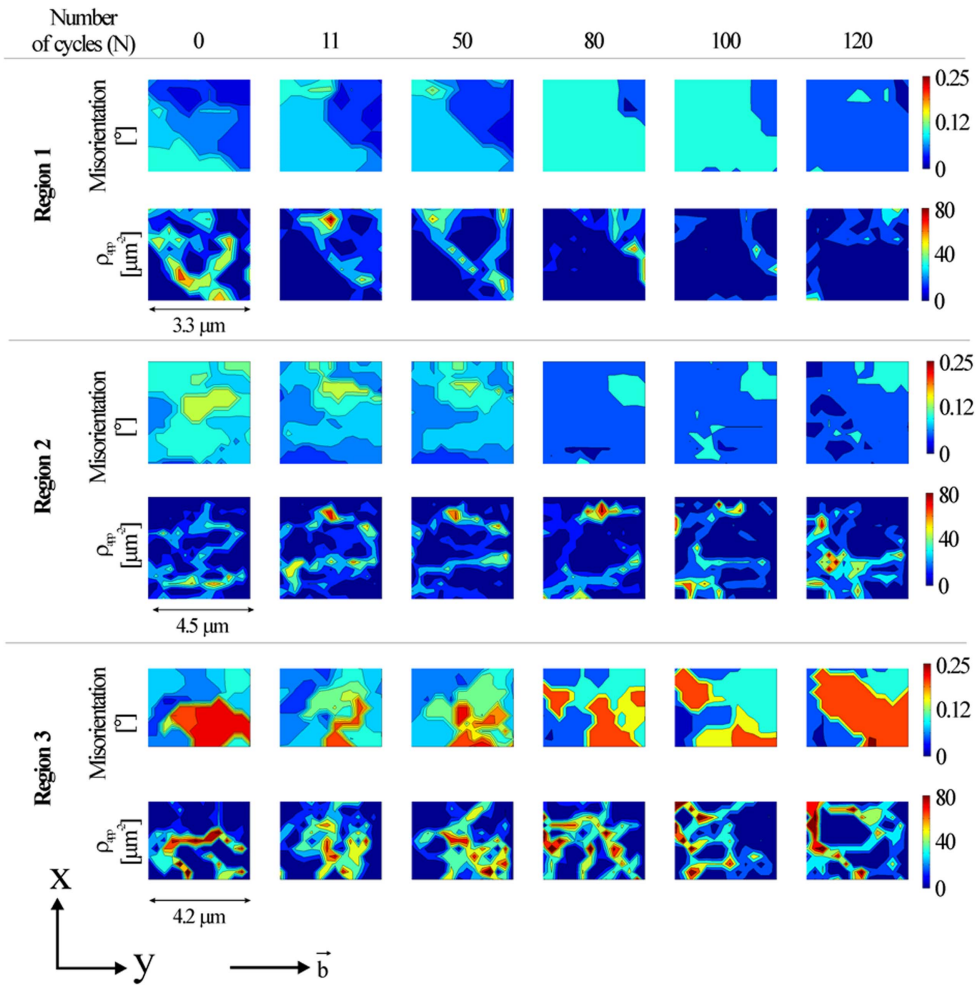

Figure 1. Evolution of misorientation and apparent GND traces upon cycling in three regions, reproduced with permission from [16], copyright 2016 Elsevier. For explanation see text.

matrix was determined by indexing each diffraction pattern collected in an area of $10 \times 25\ \mu m^2$ with a step size of 300 nm. Afterwards the distribution of lattice curvature was calculated by computing the change in misorientation of two neighboring points as suggested in [19]. Assuming small elastic strains, rotation and/or elastic strain gradients, Nye's formula was used to relate lattice curvatures to GND density components [20]. From there, the apparent GND density [21] was calculated by summing the accessible dislocation density tensor components divided by the Burgers vector (see figure A1). Further details about mechanical test and data analysis can be found in [16].

Before cycling the sample contained a certain amount of dislocations due to sample preparation and sample handling. It can be assumed that because of single slip orientation, some of these dislocations are mobile, while others are immobile. Figure 1 shows the evolution of misorientation and apparent GND density in three different regions during

cycling [16]. These regions are sections that are part of a larger region as in figure A1 and in [16].

- Region 1 contains at the beginning sub-regions with only very small variations in misorientation, whose borders are marked by non-zero values of apparent GND density traces. These initial misorientations homogenize during cycling and the apparent GND traces disappear.
- Region 2 includes a higher initial misoriented area of approximately 0.14° that slowly disappears during cycling. Initially apparent GND traces mark the perimeter of this misoriented area but there are also several other GND traces contained in region 2 connected with lower misoriented areas. After 120 cycles, the absolute values in the misorientation map are similar to the one of region 1. There are, however, several apparent GND traces still present and their densities are in fact higher than those before cycling. Note that the traces are mainly located in the area with initial low misorientation.
- Region 3 shows initially a highly misoriented area of 0.22°. This area is surrounded by high density apparent GND traces. During cycling, the misoriented area fragments but never vanishes. During the last cycles, it reconstructs and expands, remaining marked by high density apparent GND traces.

It is interesting to note that the three regions contain initially non-negligible apparent GND density traces of the order of 60 μm^{-2} or higher. Yet the evolution in these regions after 120 cycles is very different: homogenization with no final apparent GND traces (region 1), increase in number and density of apparent GND traces (region 2) or reorganization of traces while keeping high density values (region 3) can be observed. The results suggest a time evolution in dislocation patterning during the initial fatigue stages that is affected by the presence of pre-existing dislocation structures and their mobility during cycling.

Here, the effect of pre-existing dislocation agglomerations, in the following referred as 'cluster of immobile dislocations', on the microstructural evolution is studied during cyclic fatigue. A continuum dislocation-based model in CPFEM framework is employed [15, 22], allowing access to both dislocation density and crystal lattice rotation evolution. Cyclic simulations in a volume of $5 \times 5 \times 1$ μm^3 are carried out, showing formation and evolution of GND walls formed around the dislocation cluster. The effect of the initial density of immobile dislocations in the cluster and the ratio between mobile and immobile dislocation densities on the formation and evolution of GND walls is investigated. The different simulations are discussed in relation to the experimental observations shown in figure 1.

2. Computational method

2.1. The CPFEM

This computational method is based on the decomposition of the deformation gradient **F** into an elastic and plastic part: $\boldsymbol{F} = \boldsymbol{F}_e \cdot \boldsymbol{F}_p$. The plastic deformation gradient evolves based on the activity of all the slip systems of the FCC crystal [23]:

$$\dot{\boldsymbol{F}}_p \cdot \boldsymbol{F}_p^{-1} = \sum_{\alpha=1}^{12} \dot{\gamma}_p^{\alpha} \boldsymbol{m}^{\alpha} \otimes \boldsymbol{n}^{\alpha}, \tag{1}$$

where $\boldsymbol{m}^{\alpha}$ and $\boldsymbol{n}^{\alpha}$ are the slip direction and slip plane normal of the slip system α. In dislocation-based models, the plastic strain rate $\dot{\gamma}_p^{\alpha}$ is given by Orowan's law:

Table 1. Rate equations for the different dislocation processes considered in the model. c_e is the character of edge dislocations (e^+or e^-), c_s is the character of screw dislocations (s^+or s^-). The bar over c_e and c_s indicates opposite Burgers vector. $\hat{d}_e$ and $\hat{d}_s$ are the characteristic annihilation distance for edge and screw dislocations. $\bar{l}_c$ is an average dislocation segment length and β is the cross slip coefficient.

Dislocation process	Rate equation
Dislocation multiplication	$\dot{\rho}^{\alpha}_{c_e,\mathrm{mult}} = \frac{\rho^{\alpha}_{c_e,s+}\lvert v^{\alpha}\rvert}{\bar{l}_c} + \frac{\rho^{\alpha}_{c_e,s-}\lvert v^{\alpha}\rvert}{\bar{l}_c}$
	$\dot{\rho}^{\alpha}_{c_s,\mathrm{mult}} = \frac{\rho^{\alpha}_{e+,c_s}\lvert v^{\alpha}\rvert}{\bar{l}_c} + \frac{\rho^{\alpha}_{e-,c_s}\lvert v^{\alpha}\rvert}{\bar{l}_c}$
Dislocation annihilation	$\dot{\rho}^{\alpha}_{c_e,\mathrm{ann}} = -4\hat{d}_e\rho^{\alpha}_{e+}\rho^{\alpha}_{e-}\lvert v^{\alpha}\rvert$
	$\dot{\rho}^{\alpha}_{c_s,\mathrm{ann}} = -4\hat{d}_s\rho^{\alpha}_{s+}\rho^{\alpha}_{s-}\lvert v^{\alpha}\rvert$
Cross slip	$\dot{\rho}^{\alpha}_{c_e,c_s,\mathrm{CS}} = \frac{\beta\lvert v^{\alpha}\rvert}{b}(\rho^{\alpha}_{s+} + \rho^{\alpha}_{s-})$

$$\dot{\gamma}^{\alpha}_{p} = \rho^{\alpha}_{\mathrm{m}} v^{\alpha} b, \tag{2}$$

where $\rho^{\alpha}_{\mathrm{m}}$ is the mobile dislocation density on the slip system α, b is the Burgers vector and v^{α} is the dislocation velocity. In this work the DAMASK subroutine is used [24], which allows implementing user-defined rate equations for the dislocation densities.

2.2. Dislocation-based rate equations

The dislocation-based rate equations used in this work have been developed specifically for cyclic fatigue and they are able to reproduce dislocation structures [15]. The model has eight state variables for every slip system. Four of them (indicated by ρ_{e+}, ρ_{e-}, ρ_{s+} and ρ_{s-}) represent straight edge and screw dislocation lines, which have no curvature. Other four densities (indicated by $\rho_{e+,s+}$, $\rho_{e+,s-}$, $\rho_{e-,s+}$, and $\rho_{e-,s-}$) are dislocation segments connecting straight edge and screw dislocations and they are curved, therefore they are responsible for the dislocation multiplication [25]. This particular choice of state variables is motivated by the geometry of the vein-channel structure expected in fatigued single slip oriented copper single crystals. Veins are constituted of straight edge dislocations (ρ_{e+} and ρ_{e-}), while screw dislocations (ρ_{s+} and ρ_{s-}) glide in the middle of channels and have low curvature. The dislocation segments connecting edge and screw dislocations have the highest curvature. If ρ_c is the density of dislocations with character c, its time evolution equation is given by:

$$\dot{\rho}^{\alpha}_{c} = \dot{\rho}^{\alpha}_{c,\mathrm{mult}} + \dot{\rho}^{\alpha}_{c,\mathrm{ann}} + \dot{\rho}^{\alpha}_{c,\mathrm{CS}} - \nabla\cdot(\vec{v}_c\rho_c), \tag{3}$$

where each term models a specific dislocation process, such as multiplication, annihilation and cross slip, as defined in table 1. The last term in equation (3) describes the disloation fluxes and the direction of $\vec{v}_c$ is perpendicular to the dislocation line.

2.3. Dislocation kinetics and interactions

The relation between dislocation velocity and resolved shear stress is assumed linear [15, 26], and the stress to move dislocations is given by the sum of Peierls stress ($\tau_{\mathrm{P}} = 0.5$ MPa for copper [27]) and threshold stress:

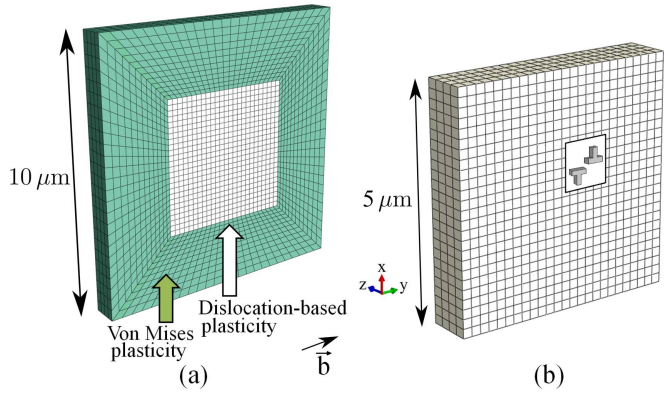

Figure 2. (a) Representative volume and mesh. (b) Part of the representative volume where the dislocation-based plasticity is used and position of the dislocation cluster.

$$\tau_{\text{th}}^{\alpha} = Gb\left(\sum_{\eta=1}^{12}\xi^{\alpha\eta}\rho^{\eta}\right)^{1/2}, \tag{4}$$

where ρ^{η} is the total dislocation density on the slip system η and the FCC interaction coefficients $\xi^{\alpha\eta}$ [28] are used. The simulations in our manuscript are carried out in strain control (see section 2.4); therefore, the characteristic length travelled by one dislocation does not depend on the specific velocity–stress equation used according to Orowan's law. Under these conditions, the velocity can be approximated as linear function of the resolved shear stress, allowing to be computationally efficient. The long-range dislocation–dislocation interactions are also included in the CPFE method which uses dislocation fluxes [29, 30], as described by the last term in equation (3). These are due to the motion of dislocations, which can travel through neighboring integration points of the finite element mesh, inducing plastic deformation. Gradients of the plastic slip are caused by obstacles for the dislocation motion (e.g. dislocation structures). Therefore, compatible elastic strains and the corresponding equilibrated stresses will be present in order to satisfy strain compatibility and stress equilibrium. These stresses will correspond to the stress field of GNDs.

Several existing methods take into account the long-range internal stresses. In the model developed by Groma *et al* [31], for instance, long-range dislocation–dislocation interactions are calculated by averaging the stress field of individual dislocations over a statistical ensemble and the model uses a constant external stress field. On the other hand, models that do not include dislocation fluxes between integration points use a non-local backstress measure [32]. This backstress term is subtracted from the effective shear stress in order to take into account the long range stress induced by GNDs, and the GND density is directly calculated from the gradient of the plastic slip. The major differences between these models and the CPFE method used in the present paper are that here arbitrary stress fields and boundary conditions can be modelled and that GNDs are induced by gradients of the dislocation flux.

2.4. Simulated volume and boundary condition

The representative volume used in the simulations is a parallelepiped with dimensions $10 \times 10 \times 1\ \mu\text{m}^3$ along the x, y and z axes, as shown in figure 2(a). The central part ($5 \times 5 \times 1\ \mu\text{m}^3$) is modelled using the dislocation-based plasticity model explained in section 2.2, while the surrounding is described by von Mises plasticity [33]. In that volume,

Table 2. Parameters of the von Mises model for copper [34, 35].

Parameter	Value	Unit
$\dot{\gamma}_o$	1×10^{-10}	s^{-1}
n	20	
$g(t=0)$	10	MPa
g_∞	28	MPa
h_o	100	MPa
α	2.5	

the plastic strain rate is given by:

$$\dot{\gamma} = \dot{\gamma}_o (\sqrt{J_2}/g)^n, \tag{5}$$

where $\dot{\gamma}_o$ is a reference strain rate, n is the stress exponent and J_2 is the von Mises equivalent stress. The flow stress g evolves as:

$$\dot{g} = h_o \dot{\gamma} \, |1 - g/g_\infty|^\alpha \text{sign}(1 - g/g_\infty), \tag{6}$$

where h_o, α are parameters and g_∞ is the saturation flow stress. The parameters of the von Mises model for copper are reported in table 2.

The parameters of von Mises plasticity model are selected to match the hardening behavior of the dislocation-based plasticity model, i.e. to obtain the same saturation stress after cyclic deformation. Therefore, boundary effects may appear at the interface due to a difference of hardening behavior of the two material models as is discussed in section 3. The mesh size used is 200 nm. The cluster of immobile dislocations, with density ρ_{imm}, is placed parallel to the z axis. The dimensions of the cluster are $1 \times 1 \times 1$ μm^3 along the coordinate axes and its position in the x–y plane is displaced 0.5 μm with respect to the center of the geometry, as shown in figure 2(b).

Periodic dislocation fluxes are used on the surface of the dislocation-based plasticity region. The displacement is imposed along the external surface in order to induce pure shear in the central region, as shown in figure 3. In this configuration, the crystal is oriented for single slip with the normal of the (111) primary slip plane parallel to the x-axis and the primary Burgers vector parallel to y-axis. The function $U(t)$ is chosen to simulate the experimental strain amplitudes applied in [16] and it varies linearly between two extreme values depending on the cycle number N in a time interval $\Delta t = 0.2$ s, as shown in figure 4. The strain rate ($\dot{\gamma_{xy}}$) is around $0.05 \div 0.1$ s^{-1}.

Simulations are carried out with different initial ρ_{imm} in the cluster and different ratios of initial mobile (ρ_{mob}) to immobile dislocation densities, as reported in table 3. The different simulations are indicated by 'Im3-R0.33', 'Im3-R0.05', 'Im20-R0.05' and 'Im100-R0.05'. The number after 'Im' is the initial ρ_{imm} in μm^{-2} and the number after 'R' is the ratio. Initial random fluctuations with a value up to 10% are added to the mobile dislocation densities. These dislocation densities are chosen in order to make a systematic investigation of the effect of initial immobile dislocation clusters during early fatigue. Besides, they create similar rotation values ($\leqslant 0.2°$), as the experimental values shown in figure 1 and reported in [16], allowing easy comparison.

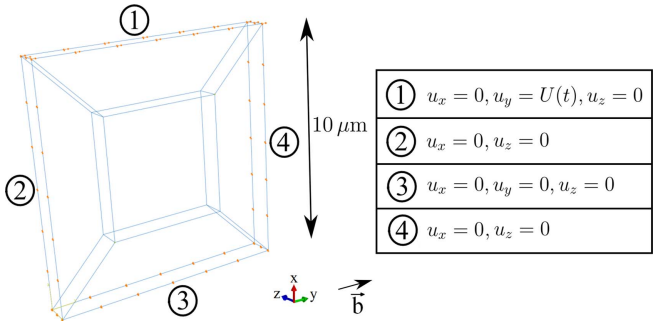

Figure 3. Boundary conditions.

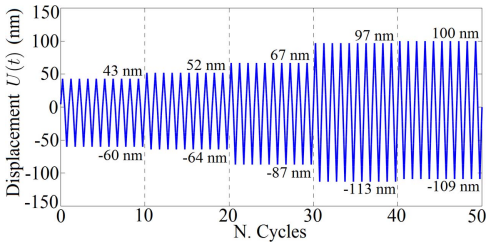

Figure 4. Maximum and minimum values of the applied displacement as a function of the number of cycles *N*.

Table 3. Initial values of the dislocation densities.

Initial dislocation densities ($t = 0$) (μm^{-2})	Im3-R0.33	Im3-R0.05	Im20-R0.05	Im100-R0.05
ρ_{imm}	3	3	20	100
ρ_{e+}, ρ_{e-}, ρ_{s+}, ρ_{s-}	1	0.15	1	5
$\rho_{e+,s+}$, $\rho_{e+,s-}$, $\rho_{e-,s+}$, $\rho_{e-,s-}$	0.02	0.003	0.02	0.1

3. Results and discussion

3.1. Influence of the ratio between the initial mobile and immobile densities

The effect of the ratio between mobile and immobile dislocation densities on the microstructural evolution is investigated by examining the edge GND density ($\rho_{e+} - \rho_{e-}$) of the primary slip system during the early fatigue cycles where the displacement amplitude is kept constant ($N < 10$). The pre-existing cluster of immobile dislocations represents an initial heterogeneity and it obstacles the motion of primary edge dislocations along the Burgers vector direction, creating a GND wall. When the load is reversed, edge dislocations move along opposite direction, but the GND wall does not fully disappear even if the applied displacement is zero ($U(t) = 0$). The reason behind is that the dislocations in the forming GND wall increase the threshold stress τ^1_{th}, which during reverse loading prevents part of the GNDs to move to their original position. That is why the evolution of τ^1_{th} during the early cycles is analyzed in parallel.

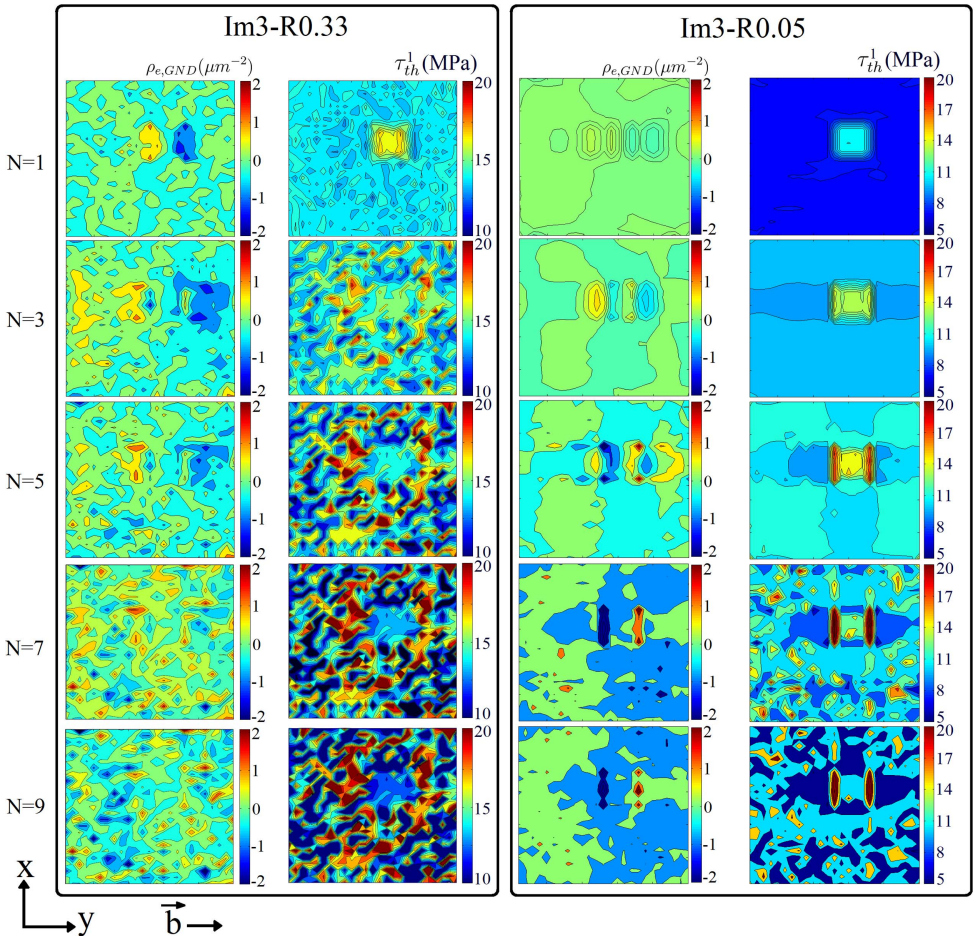

Figure 5. Relationship between the geometrically necessary edge dislocation density ($\rho_{e+} - \rho_{e-}$) and the threshold stress on the primary slip system for two different values of the mobile dislocation density.

Figure 5 shows the evolution of edge GND density ($\rho_{e+} - \rho_{e-}$) of the primary slip system and of τ^1_{th} of Im3-R0.33 and Im3-R0.05, where the following is observed:

- In Im3-R0.33 GND walls are already formed after one cycle. More cycles are required to observe wall formation in Im3-R0.05 due to a lower initial ρ_{mob}. After the first cycle both cases show that τ^1_{th} is higher where the initial immobile cluster is located than in the surroundings. The absolute τ^1_{th} values in Im3-R0.33 are higher than in Im3-R0.05.
- After 3 cycles GND walls are still visible for both cases, but the GND walls in Im3-R0.33 start dissociating. The analysis of τ^1_{th} distribution shows that in Im3-R0.33 the surroundings of the initial cluster have patterned spots with high values. In the Im3-R0.05 case, on the other hand, the τ^1_{th} distribution is still higher in the immobile cluster and rather uniform in the surroundings.
- From cycles 5 to 9 the evolution in both cases is very different. In the case of higher initial ρ_{mob} (Im3-R0.33), the GND walls completely dissociate and the values of τ^1_{th} in the patterns increase, as well as the average value. On the other hand, in the low initial ρ_{mob}

case (Im3-R0.05) the GND walls become very pronounced and the corresponding GND density increases upon cycling. The threshold stress τ^1_{th} shows maximum values at the interfaces of the immobile cluster where edge dislocations are being accumulated. From cycles 7 to 9, dislocation multiplication starts also getting noticeable in the initially-cluster-free areas (distributed spots with high τ^1_{th} values) but the pattern is less pronounced than in Im3-R0.33 case.

These results indicate that stable GND walls form if τ^1_{th} is higher inside the immobile cluster and at its interface with the surrounding region (Im3-R0.05). If the initial ρ_{mob} is high enough (Im3-R0.33), dislocation multiplication leads also to higher values of τ^1_{th} in the surrounding region. Thus, the forming fatigue dislocation structures become the main obstacles to the motion of mobile dislocations rather than the initial immobile dislocation cluster.

3.2. Influence of the initial immobile density

In this section the microstructural evolution of Im3-R0.33 and Im3-R0.05 after further cycles is investigated. Concurrently, Im20-R0.05 and Im100-R0.05 are analyzed to determine the effect of the initial ρ_{imm}. Figure 6 shows the evolution of edge GND density $(\rho_{e+} - \rho_{e-})$ of the primary slip system from cycle 10 to 50 in the four cases with the same scalebar and figure 7 shows the corresponding evolution of the average and the l^2 distance between the function $(\rho_{e+} - \rho_{e-})$ at different number of cycles. The following conclusions can be drawn:

- By comparing the averaged values after 10 cycles in figure 7, it is observed that higher initial ρ_{mob} and ρ_{imm} values lead to higher GND density values. After the initial cycles, Im100-R0.05 has the highest average edge GND density, followed by Im20-R0.05, Im3-R0.33 and finally Im3-R0.05 (initial ρ_{mob} of 5, 1, 1 and 0.15 respectively μm^{-2}). This trend is kept when applying further cycles. Interestingly, the evolution curves of Im20-R0.05 and Im3-R0.33, both having same initial ρ_{mob} but different ρ_{imm}, are almost parallel.
- In all $R = 0.05$ cases, GND walls are observed to form around the initial cluster after 10 cycles independently of initial ρ_{imm}. For the low initial ρ_{imm} (Im3-R0.05), the walls are fragmented though. In the Im3-R0.33 case, the walls have already been dissociated (see figure 5 and corresponding explanation).
- The evolution of the formed GND walls depends strongly on ρ_{imm} and R. For low ρ_{imm} (Im3-R0.05) the fragmented walls show a formation of a substructure with alternating edge GND density $(\rho_{e+} - \rho_{e-})$ in each wall. This substructure formation occurs from 10 cycles on. For high ρ_{imm} values (Im100-R0.05) a higher number of cycles is required before observing partial dissociation of walls after 40 cycles. In the particular case of Im20-R0.05, the formed GND walls are stable during the applied cycles.
- In all four cases, the GND distribution remains stable after the displacement jump at 40 cycles. Actually, the evolution of the curves in figure 7 show stability on all four cases.
- After 50 cycles, each case has a particular edge GND density $(\rho_{e+} - \rho_{e-})$ distribution.

These results indicate that the initial ρ_{imm} has an effect on the evolution of GNDs. In order to gain a better understanding, the τ^1_{th} distribution is examined. Figure 8 shows the threshold stress τ^1_{th} of the primary slip system as a function of the number of cycles N for Im3-R0.33, Im3-R0.05, Im20-R0.05 and Im20-R0.05 cases from cycle 10 to 50 with the same scalebar and the corresponding evolution of the average and the l^2 distance in figure 9. It is observed that:

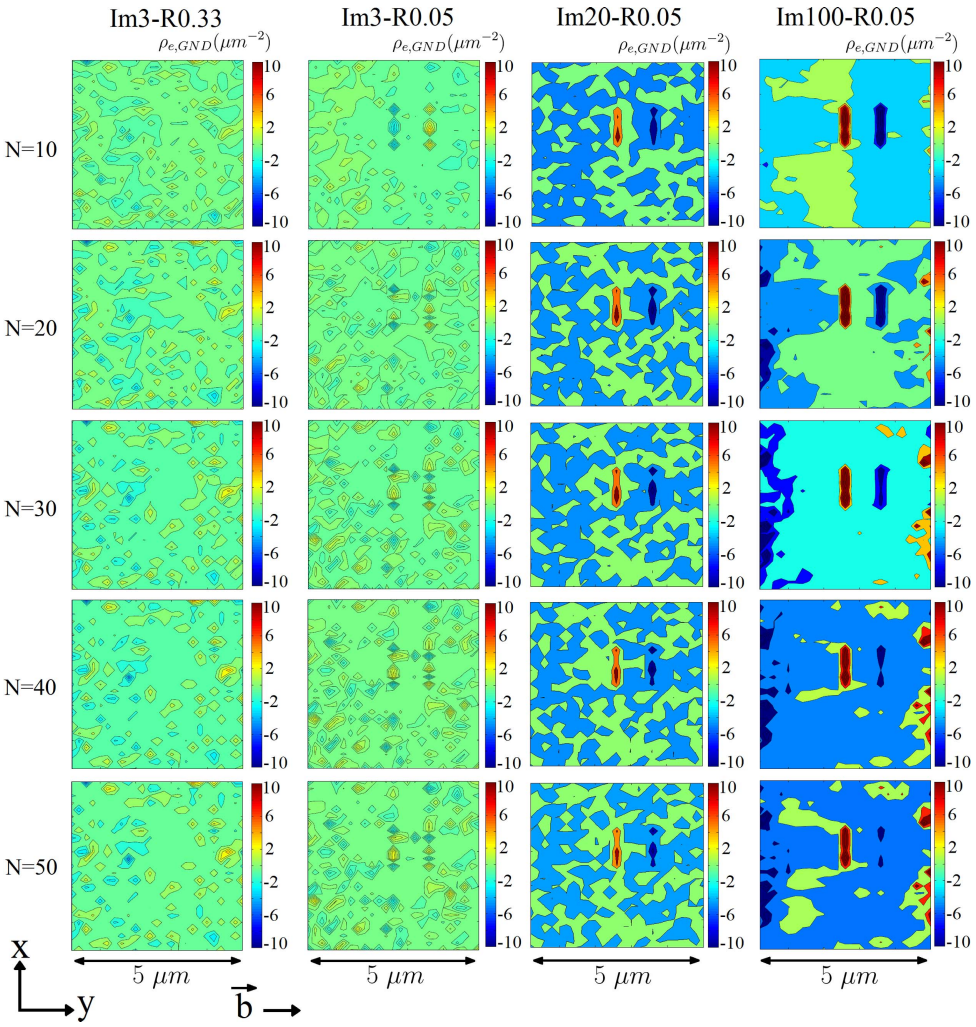

Figure 6. Geometrically necessary edge dislocations ($\rho_{e+} - \rho_{e-}$) averaged over depth (z-axis) at different number of cycles N and for different mobile and immobile dislocation densities with same scalebar.

- The values of the patterned τ^1_{th} distribution of Im3-R0.33 already observed at earlier cycles (see figure 5 and corresponding explanation) increase upon further cycling as it can be noticed in figure 8. On the other hand, the trend of the average curve in figure 9 is rather steady with slight increase during the last 10–20 cycles even if there is no evident change in the distribution.
- For the same ρ_{imm} but lower initial ρ_{mob} (Im3-R0.05), τ^1_{th} has higher values at the interface of the immobile cluster and patterning in the surrounding region becomes observable. The averaged value is however lower than in Im3-R0.33. The applied cycles do not change the τ^1_{th} distribution but slightly increases the averaged values. Note that the substructure in the GND walls forms with constant τ^1_{th} values.

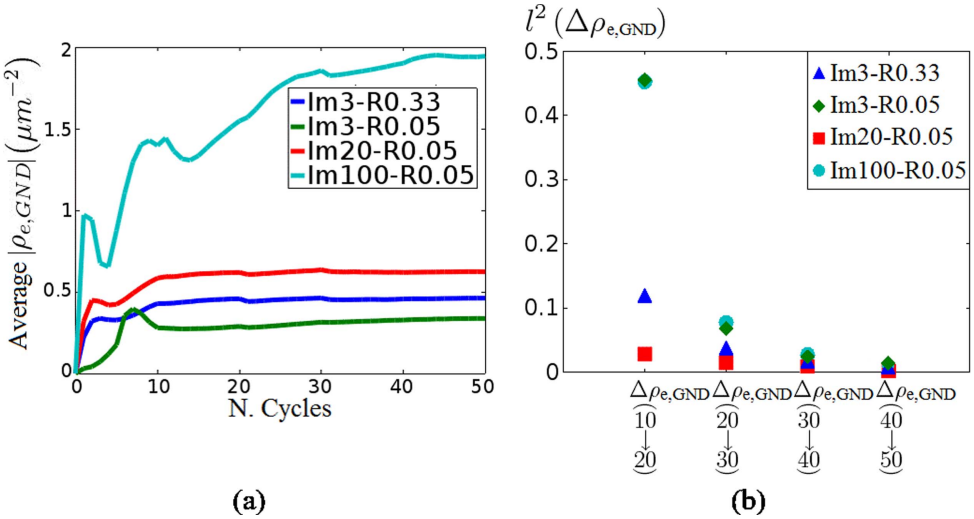

Figure 7. Evolution of average (a) and l^2 distance (b) of the geometrically necessary edge dislocations $(\rho_{e+} - \rho_{e-})$ for different mobile and immobile dislocation densities. $l^2(\Delta\rho_{e,\mathrm{GND}}(10 \rightarrow 20))$ indicates the distance between the normalized function $(\rho_{e+} - \rho_{e-})$ at cycle 20 and the same function at cycle 10.

- The qualitative behavior of Im20-R0.05 is analogue to the early stages of Im3-R0.05 (see corresponding evolution during first cycles in figure 5). Dislocations accumulate at the interface of the immobile cluster where τ^1_{th} is highest and GND walls form. Patterning also evolves in the surrounding region. In fact it is more evident than in Im3-R0.05 due to higher initial ρ_{mob}. Note that the τ^1_{th} values inside the cluster are still high and do not lower as it was observed in Im3-R0.05 from cycle 5 to 9 (see figure 5). Interestingly and similar to what it was observed in figure 7, the evolution curves of Im20-R0.05 and Im3-R0.33, both having same initial ρ_{mob} but different ρ_{imm}, are almost identical.
- In the extreme case of Im100-R0.05, the behavior of τ^1_{th} is similar to the first few cycles of Im3-R0.05 (see figure 5) but with higher absolute values. During the 50 cycles, τ^1_{th} is maximum in the cluster, the surrounding region of the cluster shows low and uniform τ^1_{th} and no pattern formation is observed. Note that the boundary effects are noticeable in this case due to the difference of the hardening behavior of the two material models at the interface between dislocation based plasticity and von Mises plasticity regions (as described in section 2.4. In fact, similar boundary effects can be found in figure 6 localized on the first and/or second layer of elements, mainly close to the right and left boundaries. The reason behind these dislocation density walls and high τ^1_{th} is the inhomogeneous stress field created upon cycling at the interface in the case of high initial dislocation density, which creates an inhomogeneous dislocation velocity field as shown and described in figure 10.

The reason behind the presence or absence of pattern formation is related to the initial ρ_{mob} and to the dislocation velocity, to satisfy the Orowan's law—equation (2). Figure 10 shows the dislocation velocity at cycle 50 for the four studied cases. The following conclusions can be drawn:

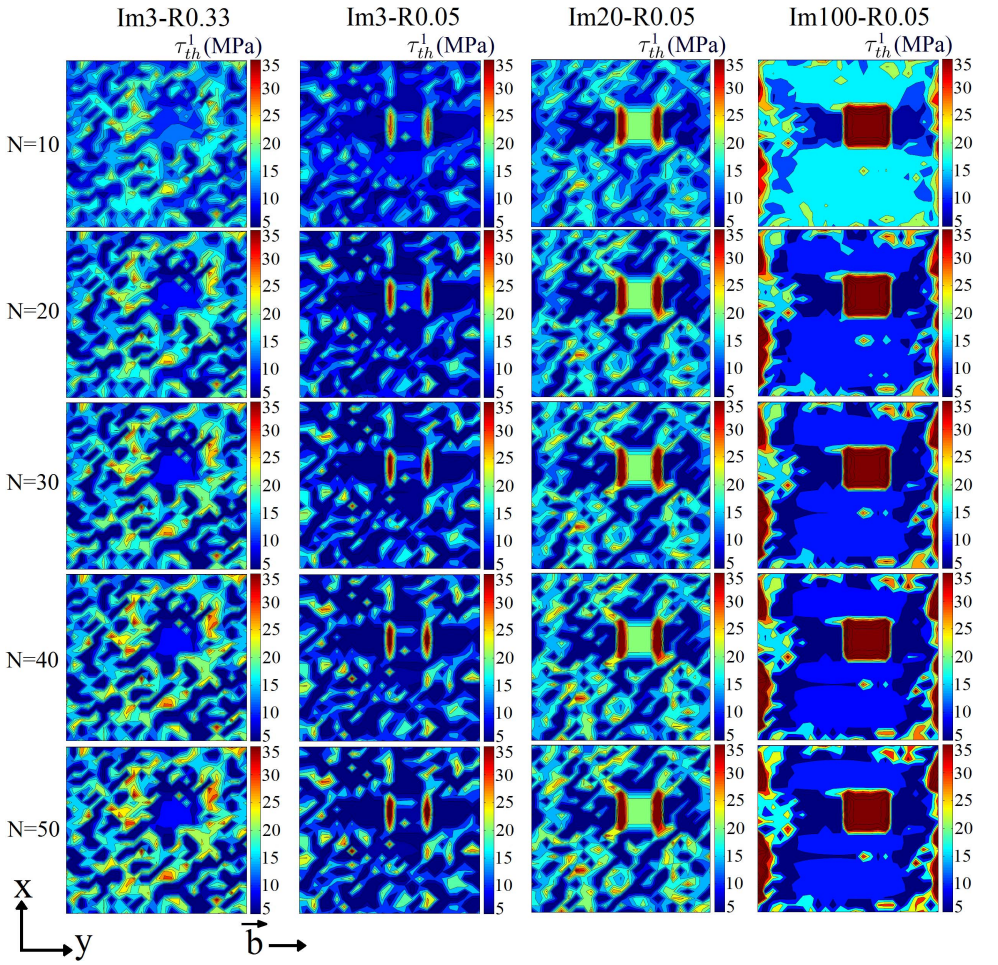

Figure 8. Threshold stress on the primary slip system at different number of cycles N and for different mobile and immobile dislocation densities.

- In both Im3-R0.33 and Im3-R0.05, for which the initial ρ_{imm} is low, the region where the cluster is located shows non-zero velocity meaning that mobile dislocations were able to penetrate in it. In Im3-R0.05, there are more areas in the surrounding of the cluster with higher velocity. This can be explained with Orowan's law in equation (2) because the ρ_{mob} in that case is lower. In fact, the presence of high velocity regions at the interface of the cluster in Im3-R0.05 leads to the formation of substructure in the GND walls observed in figure 6.
- The velocity field of Im20-R0.05 shows zero velocities inside the initial immobile cluster. Thus mobile dislocations could not get inside the cluster. The velocity field in the surrounding is however similar to that of Im3-R0.05 where patterns are formed in the surrounding of the cluster. The velocity values at the interface of the cluster are also high and that is why GND walls are formed, since GNDs tend to move there.
- In Im100-R0.05 most of the simulated region has an almost zero velocity due to the high initial mobile density. In fact, Orowan's law—equation (2)—gives a value of the dislocation velocity which decreases if ρ_{mob} is higher. This leads to regions with lower

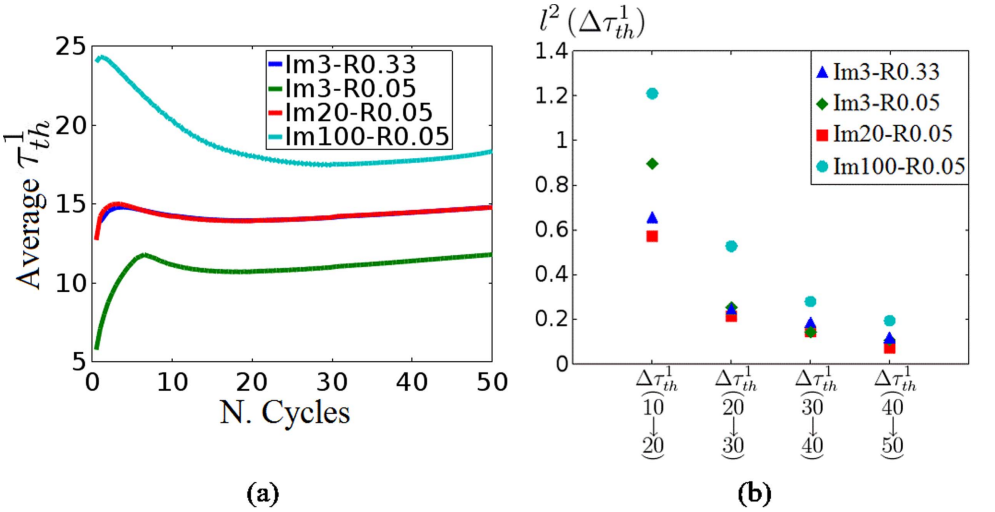

Figure 9. Evolution of average (a) and l^2 distance (b) of the threshold stress on the primary slip system for different mobile and immobile dislocation densities. $l^2(\Delta\tau^1_{\text{th}}(10 \rightarrow 20))$ indicates the distance between the normalized function τ^1_{th} at cycle 20 and the same function at cycle 10.

multiplication rate and less formation of dislocation structures around the immobile cluster. As a consequence there is no pattern formation in the surroundings but only on the walls of the cluster, which acts as main and only obstacle during fatigue.

These results show that the formation and evolution of GND walls formed around the initial immobile cluster depends not only on the ratio between the mobile and immobile dislocation density as shown in section 3.1, but also on the absolute values of the densities. For a given ratio, the initial values determine the microstructural evolution: either GND walls form and show the formation of substructure (Im3-R0.05); eventually stable GND walls form at the interface but pattern formation in the surroundings is not prevented (Im20-R0.05); or the cluster acts as a dominant obstacle for dislocation motion and inhibits pattern formation in the surrounding (Im100-R0.05).

In contrast to simulations, experimentally edge GND dislocation density and threshold stress are seldom accessible. From the 2D rotational fields measured with transmission Laue diffraction or with EBSD, six components of the lattice curvature tensor are accessible (κ_{ix} and κ_{iy} with $\{i\} = \{x, y, z\}$). They can be used to calculate an apparent density of GNDs [21] (see figure A1). These curvatures can be also calculated with the CPFE method. Figure 11 shows the evolution of apparent GND density as a function of the number of cycles N for the four cases with same scalebar and figure 12 shows the corresponding evolution of the average and the l^2 distance:

- In Im3-R0.33 the traces of the apparent GND density at cycle 10 are not well defined but rather disperse. Upon cycling the density of the traces increases but the distribution maintains random. In fact the presence of the initial cluster remains unnoticed and after 50 cycles it has the lowest average ρ_{app} value.
- In Im3-R0.05 the initial defect cluster is predominant during the first 20 cycles: the high density apparent GND traces are mainly localized in the surrounding of the cluster.

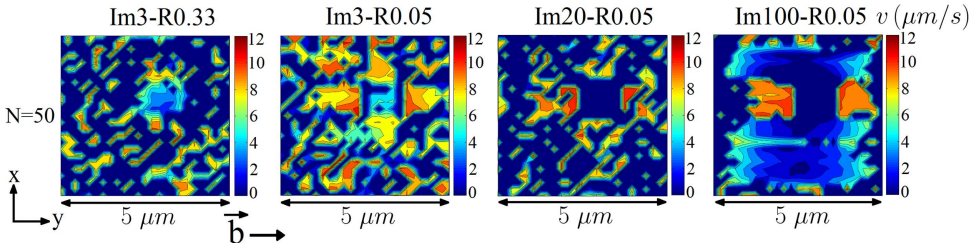

Figure 10. Velocity at cycle 50 and for different mobile and immobile dislocation densities with same scale bar.

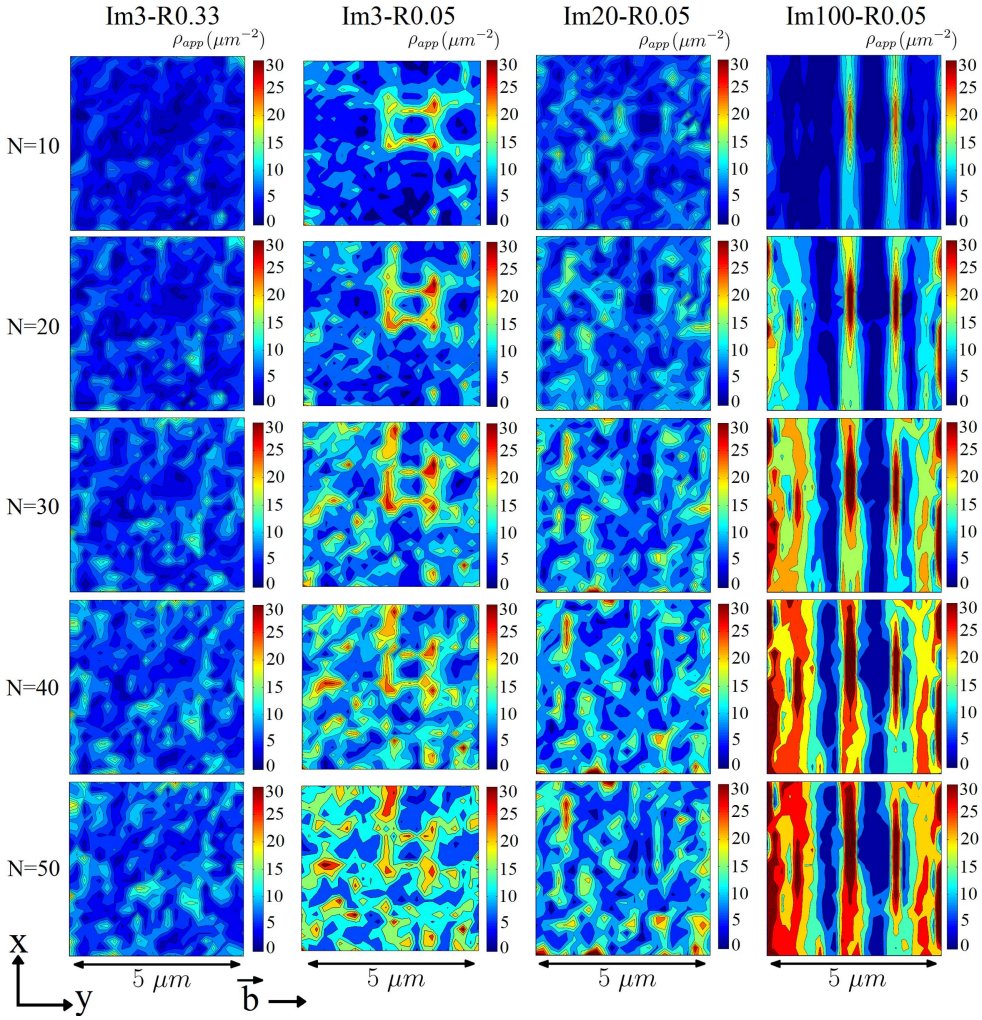

Figure 11. Apparent GND density at different number of cycles N and for different value of the dislocation densities.

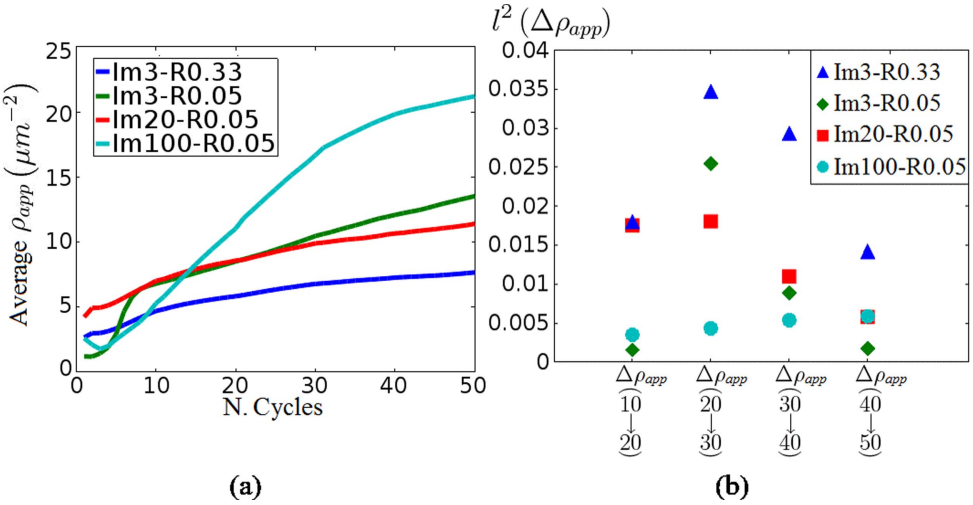

Figure 12. Evolution of average (a) and l^2 distance (b) of the apparent GND density for different mobile and immobile dislocation densities. $l^2(\Delta\rho_{\text{app}}(10 \rightarrow 20))$ indicates the distance between the normalized function ρ_{app} at cycle 20 and the same function at cycle 10.

During the last 30 cycles, the walls are still visible but the initially defect free areas also start showing high apparent GND traces visible through patterning.

- In Im20-R0.05, the distribution of the apparent GND traces after 10 cycles resembles the one of Im3-R0.05 at cycle 30-40 but with much lower ρ_{app} values. The presence of the immobile cluster is noticeable by apparent GND walls but the surroundings have also high apparent GND traces. After more cycles the area where the cluster was located stays free of GNDs. The GND-free region is of the same size as other areas where no apparent GND traces have been accumulated. After 50 cycles, the average ρ_{app} of Im20-R0.05 is higher than that of Im3-R0.33. Similar to what it was observed in figure 7, during cycling the curve is parallel though. Surprisingly, after 50 cycles, Im3-R0.05 has higher average ρ_{app} than Im20-R0.05, in spite of the fact that the former has same R but overall lower ρ_{imm} and ρ_{mob}.
- When the initial immobile dislocation density is high enough (Im100-R0.05) the initial defect cluster is dominant during all the applied cycles. Well pronounced and high GND apparent density walls are formed after 10 cycles which remain stable. Similar to what it was observed in figure 8 boundary effects are evident.
- Figure 12 also shows that in all four cases the average ρ_{app} value is constantly increasing upon cycling. On the other hand, average $|\rho_{\text{edge}}|$ and τ^1_{th} have reached almost stationary phase according to figures 7 and 9.

4. Conclusions

The influence of immobile dislocation clusters on the formation of lattice rotation during fatigue has been studied with CPFEM simulations in which dislocation-based rate equations developed specifically for cyclic fatigue had been implemented. It has been shown that both

Table 4. Summary of the results.

	$\rho_{e+} - \rho_{e-}$	τ^{1}_{th}	ρ_{app}
Im3-R0.33	Wall formation and their dissociation during first cycles	Pattern formation around the initial cluster	Random pattern formation
Im3-R0.05	Wall formation and posterior substructure formation	Formation of walls and pattern around the cluster	Formation of walls and pattern around the cluster
Im20-R0.05	Formation of stable walls	Formation of walls and pattern around the cluster	Random pattern formation
Im100-R0.05	Wall formation and partial dissociation at higher cycles	Strong cluster	Strong walls

the initial ρ_{imm} in the cluster and the ratio between ρ_{mob} and ρ_{imm} have an effect on the formation of GND walls around the pre-existing defects and on their evolution. Table 4 summarizes the main results observed in this work. Briefly, the complete dissociation of edge GND walls takes place only with high ρ_{mob} to ρ_{imm} ratios ($R = 0.33$). For lower ratios ($R = 0.05$), the evolution of the GND walls depends on the initial values which will determine whether substructures are formed, whether the walls are stable or whether they dissociate. The threshold stress τ^{1}_{th} will show walls at the interface of the immobile cluster only when GND walls are not dissociated (see all $R = 0.05$ cases), but similar threshold stress τ^{1}_{th} distributions do not necessarily lead to same ($\rho_{e+} - \rho_{e-}$) distribution (compare Im3-R0.05 and Im20-R0.05). On the other hand, the apparent GND density is shown to be more correlated with the threshold stress τ^{1}_{th} than with the edge GND density: both of them exhibit formation of patterning in the surroundings of the cluster for low ρ_{mob} values (Im3-R0.33, Im3-R0.05 and Im20-R0.05), while for high ρ_{mob} values (Im100-R0.05) only walls are observed. Depending on the initial values and ratios, the presence of the cluster in the ρ_{app} maps can remain invisible (see Im3-R0.33 or Im20-R0.05). It is also important to notice that the values of computed ρ_{app} are higher than the values of ($\rho_{e+} - \rho_{e-}$). Besides average ($\rho_{e+} - \rho_{e-}$) saturates while the average of ρ_{app} increases upon further cycling.

The behavior of the simulated dislocation structures gives insight into the microstructural evolution of the three experimentally measured regions displayed in figure 1: region 1 where pre-existing apparent GND walls disappear could be comparable to Im3-R0.33, region 2 where pre-existing apparent GND walls rearrange and pattern forms around the initially misoriented region could be equivalent to Im20-R0.05, and region 3 where the initial high density GND traces never vanish could be analogous to Im100-R0.05.

In summary, these findings illustrate the role of pre-existing dislocation structures in evolution of dislocation ensembles during cyclic fatigue and they show that apparent GND densities can be used to make a qualitative comparison with the lattice curvatures evolution measured experimentally in samples with pre-existing dislocation content.

Acknowledgments

The authors thank the Swiss National Science foundation for financial support (SNF—138240). AI-L and HVS thank the European Research Council for the advanced grant MULTIAX (339245).

Appendix

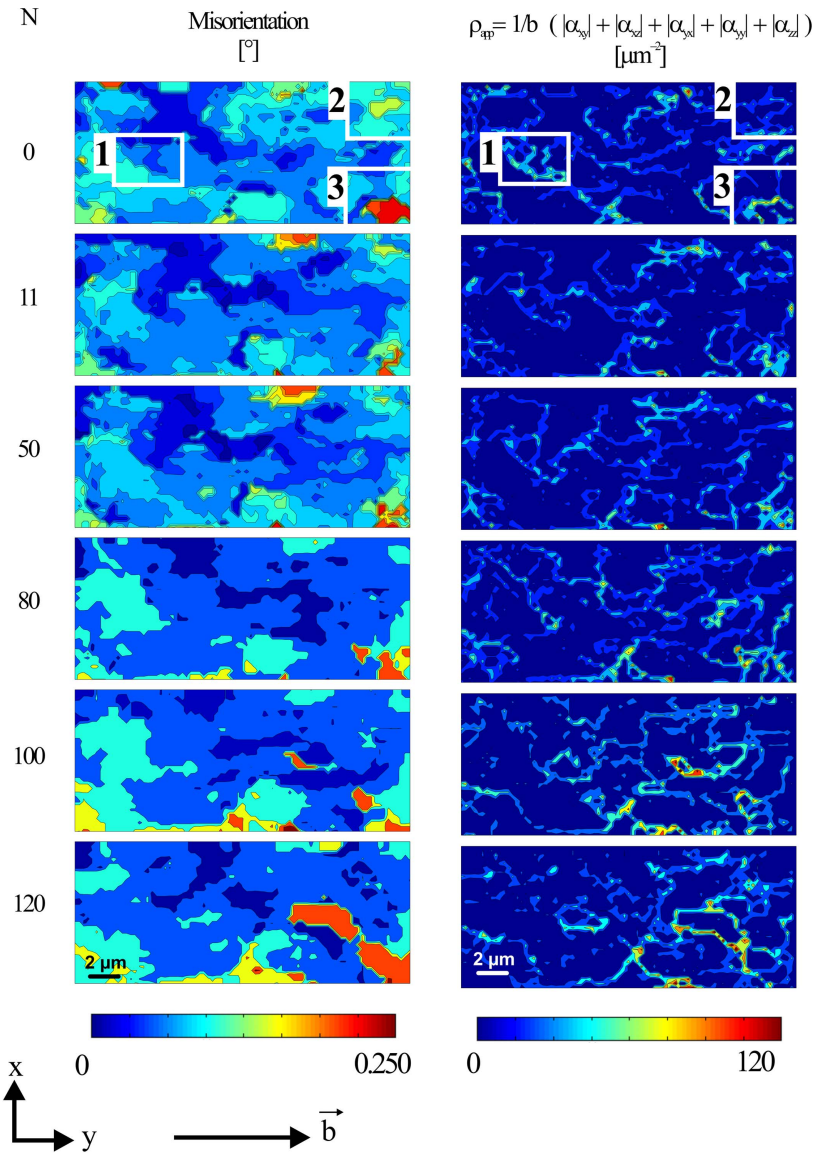

Figure A1. Evolution of apparent GND traces upon cycles, reproduced with permission from [16], copyright 2016 Elsevier. For explanation see text.

References

[1] Li P, Li S X, Wang Z G and Zhang Z F 2011 Fundamental factors on formation mechanism of dislocation arrangements in cyclically deformed fcc single crystals *Prog. Mater. Sci.* **56** 328–77

[2] Basinski Z S and Basinski S J 1992 Fundamental aspects of low amplitude cyclic deformation in face-centred cubic crystals *Prog. Mater. Sci.* **36** 89–148

[3] Arsenlis A and Parks D 1999 Crystallographic aspects of geometrically-necessary and statistically stored dislocation density *Acta Mater.* **47** 1597–611
[4] Mughrabi H and Obst B 2005 Misorientations and geometrically necessary dislocations in deformed copper crystals: a microstructural analysis of x-ray rocking curves *Z. Met.* **96** 688–97
[5] Mughrabi H 2006 Dual role of deformation-induced geometrically necessary dislocations with respect to lattice plane misorientations and/or long-range internal stresses *Acta Mater.* **54** 3417–27
[6] Hussein A M and El-Awady J A 2016 Quantifying dislocation microstructure evolution and cyclic hardening in fatigued face-centered cubic single crystals *J. Mech. Phys. Solids* **91** 126–44
[7] Xu J and Zhang G P 2014 Effects of grain size and initial immobile dislocation density on fatigue behavior of polycrystalline metals *Mater. Sci. Eng.* A **590** 194–8
[8] Lubarda V A 2004 Constitutive theories based on the multiplicative decomposition of deformation gradient: thermoelasticity, elastoplasticity, and biomechanics *Appl. Mech. Rev.* **57** 95
[9] Sandfeld S and Zaiser M 2015 Pattern formation in a minimal model of continuum dislocation plasticity *Modelling Simul. Mater. Sci. Eng.* **23** 065005
[10] Chen Y S, Choi W, Papanikolaou S, Bierbaum M and Sethna J P 2013 Scaling theory of continuum dislocation dynamics in three dimensions: self-organized fractal pattern formation *Int. J. Plast.* **46** 94–129
[11] Chen Y S, Choi W, Papanikolaou S and Sethna J P 2010 Bending crystals: emergence of fractal dislocation structures *Phys. Rev. Lett.* **105** 105501
[12] Xia S X and El-Azab A 2015 A preliminary investigation of dislocation cell structure formation in metals using continuum dislocation dynamics *IOP Conf. Ser.: Mater. Sci. Eng.* **89** 012053
[13] Xia S and El-Azab A 2015 Computational modelling of mesoscale dislocation patterning and plastic deformation of single crystals *Model. Simul. Mater. Sci. Eng.* **23** 055009
[14] Ma A, Roters F and Raabe D 2006 A dislocation density based constitutive model for crystal plasticity FEM including geometrically necessary dislocations *Acta Mater.* **54** 2169–79
[15] Grilli N, Janssens K G F and Van Swygenhoven H 2015 Crystal plasticity finite element modelling of low cycle fatigue in fcc metals *J. Mech. Phys. Solids* **84** 424–35
[16] Irastorza-Landa A, Van Swygenhoven H, Van Petegem S, Grilli N, Bollhalder A, Brandstetter S and Grolimund D 2016 Following dislocation patterning during fatigue *Acta Mater.* **112** 184–93
[17] Kysar J W, Saito Y, Oztop M S, Lee D and Huh W T 2010 Experimental lower bounds on geometrically necessary dislocation density *Int. J. Plast.* **26** 1097–123
[18] Wilkinson A J, Britton T B, Jiang J and Karamched P S 2014 A review of advances and challenges in EBSD strain mapping *IOP Conf. Ser.: Mater. Sci. Eng.* **55** 012020
[19] Pantleon W 2008 Resolving the geometrically necessary dislocation content by conventional electron backscattering diffraction *Scr. Mater.* **58** 994–7
[20] Nye J 1953 Some geometrical relations in dislocated crystals *Acta Metall.* **1** 153–62
[21] Gupta V K and Agnew S R 2010 Aa simple algorithm to eliminate ambiguities in EBSD orientation map visualization and analyses: application to fatigue crack-tips/wakes in aluminum alloys *Microsc. Microanal.* **16** 831–41
[22] Ma A and Roters F 2004 A constitutive model for fcc single crystals based on dislocation densities and its application to uniaxial compression of aluminium single crystals *Acta Mater.* **52** 3603–12
[23] Roters F, Eisenlohr P, Hantcherli L, Tjahjanto D D, Bieler T R and Raabe D 2010 Overview of constitutive laws, kinematics, homogenization and multiscale methods in crystal plasticity finite-element modeling: theory, experiments, applications *Acta Mater.* **58** 1152–211
[24] Roters F, Eisenlohr P, Kords C, Tjahjanto D D, Diehl M and Raabe D 2012 DAMASK: the düsseldorf advanced material simulation kit for studying crystal plasticity using an FE based or a spectral numerical solver *Proc. IUTAM* **3** 3–10
[25] Hochrainer T 2015 Multipole expansion of continuum dislocations dynamics in terms of alignment tensors *Phil. Mag.* **95** 1321–67
[26] Giessen E V der and Needleman A 1995 Discrete dislocation plasticity: a simple planar model *Model. Simul. Mater. Sci. Eng.* **3** 689–735
[27] Schoeck G and Krystian M 2005 The peierls energy and kink energy in fcc metals *Phil. Mag.* **85** 949–66
[28] Arsenlis A and Parks D M 2002 Modeling the evolution of crystallographic dislocation density in crystal plasticity *J. Mech. Phys. Solids* **50** 1979–2009

[29] Roters F 2011 Advanced material models for the crystal plasticity finite element method : development of a general CPFEM framework *Habilitation Thesis* RWTH Aachen http://pubman.mpdl.mpg.de/pubman/faces/viewItemOverviewPage.jsp?itemId=escidoc:2014632
[30] Arsenlis A 2004 On the evolution of crystallographic dislocation density in non-homogeneously deforming crystals *J. Mech. Phys. Solids* **52** 1213–46
[31] Groma I, Csikor F F and Zaiser M 2003 Spatial correlations and higher-order gradient terms in a continuum description of dislocation dynamics *Acta Mater.* **51** 1271–81
[32] Evers L 2004 Non-local crystal plasticity model with intrinsic SSD and GND effects *J. Mech. Phys. Solids* **52** 2379–401
[33] Peirce D, Asaro R J and Needleman A 1982 An analysis of nonuniform and localized deformation in ductile single crystals *Acta Metall.* **30** 1087–119
[34] Déprés C, Fivel M and Tabourot L 2008 A dislocation-based model for low-amplitude fatigue behaviour of face-centred cubic single crystals *Scr. Mater.* **58** 1086–9
[35] Dmitrieva O, Dondl P W, Müller S and Raabe D 2009 Lamination microstructure in shear deformed copper single crystals *Acta Mater.* **57** 3439–49